Metal-ion bridged high conductive RGO-M-MoS$_2$ (M = Fe^{3+}, Co^{2+}, Ni^{2+}, Cu^{2+} and Zn^{2+}) composite electrocatalysts for photo-assisted hydrogen evolution

Riyue Ge[a], Wenxian Li[a,e,*], Juanjuan Huo[b], Ting Liao[c,**], Ningyan Cheng[d], Yi Du[d,f], Mingyuan Zhu[a], Ying Li[a,e,**], Jiujun Zhang[e]

[a] Institute of Materials, School of Materials Science and Engineering, Shanghai University, Shanghai, 200444, China
[b] School of Environmental and Chemical Engineering, Shanghai University, Shanghai, 200444, China
[c] School of Chemistry, Physics and Mechanical Engineering, Queensland University of Technology, Brisbane, QLD 4000, Australia
[d] Institute for Superconducting and Electronic Materials (ISEM), Australian Institute for Innovation Materials (AIIM), University of Wollongong, Wollongong, NSW 2500, Australia
[e] Institute for Sustainable Energy, Shanghai University, Shanghai 200444, China
[f] BUAA-UOW Joint Research Centre and School of Physics, Beihang University, Beijing, 100191, China

ARTICLE INFO

ABSTRACT

Efficient photo-electrocatalysts for hydrogen evolution reaction (HER) are synthesized using a facile one-step hydrothermal method. With metal-ion bridges, highly dispersed molybdenum disulfide (MoS$_2$) nanolayers are vertically grown on the reduced graphene oxide (RGO) to form RGO-M-MoS$_2$ photocatalysts for HER, where M = Fe^{3+}, Co^{2+}, Ni^{2+}, Cu^{2+} and Zn^{2+}. The results show that the cross-bridging ions can modulate the MoS$_2$ growth priority and act as efficient charge transfer channels between RGO and MoS$_2$, and combine the advantages of the high conductivity of graphene with the photo-electrochemical activity of MoS$_2$. The metal-ion bridged MoS$_2$-M-RGO heterostructures demonstrate superior catalytic activity toward hydrogen evolution reaction in acid medium, evidenced by the remarkable higher catalytic current density at low overpotential compared with that of MoS$_2$-RGO without metal-ion bridge. This study provides a novel and facile route for establishing efficient composite photo-electrocatalysts for water splitting to generate hydrogen.

1. Introduction

Hydrogen (H$_2$), a carrier of high energy, offers sustainable, eco-friendly green energy for sustainable development of the world [1–4]. The sustainable way for generating H$_2$ is to split water through electrolysis cells. However, the water splitting reactions, such as the hydrogen evolution reaction (HER) at the negative electrode (cathode), and oxygen evolution reaction (OER) at the positive electrode (anode), are kinetically sluggish. To speed up the reactions, and make the electrolysis practical, electrocatalysts are necessary. Regarding HER at the negative electrode, noble metal platinum (Pt)-based electrocatalyst is considered to be the most efficient candidate due to its high catalytic activity and stability [5–7]. However, high-cost and low-abundance of Pt catalysts limit their large-scale commercial application. Therefore, tremendous efforts on developing and designing cost-effective and non-noble HER catalysts have been put on the replacement of Pt-based

catalysts in the last several decades [8–20]. Among the many non-noble metal catalyst candidates, molybdenum sulfide based materials such as MoS$_2$ have been proved to be the promising HER electrocatalysts. These catalysts have demonstrated the specific semiconducting characteristics and electrocatalytic activity based on theoretical simulations and experimental verification [8–11]. Particularly, their abundant active edge sites of two-dimensional structure and in-plane defects of nanosheet have been observed to be closely related to their HER performance [12,9–20]. Furthermore, due to their semiconductive properties, they might be used as the catalysts in photo-electrodes for H$_2$ generation [21,22].

In general, pure molybdenum sulfide compounds suffer from low conductivity for charge transfer to the active sites and then participate in the photo-electrocatalytic (PEC) reaction. In literature, high efficient molybdenum sulfide catalysts have been pursued to enhance the catalytic water splitting activity [23–32]. These studies are based on the

electronic structure modulation via element doping to decrease the charge transport energy barrier [25] and heterostructures construction [26,24–32] with good conductors to enhance the interface charge transfer. To increase the conductivity, graphene (G) and the reduced graphene oxide (RGO) have been used to composite with molybdenum sulfide compounds such as 2H-MoS$_2$ (space group No. 194: $P6_3/mmc$) for forming catalysts for HER [23,33]. As observed, graphene sheets as the support material could improve the conductivity of the composite catalysts and increase the dispersity of the active components due to its huge surface area [34]. RGO comes from the reduction of graphene oxide (GO), which is decorated by oxygen-contained functional groups by the oxidation process of graphite, including epoxy group, hydroxyl group, and carboxyl group on the surface and edge sites of the nanosheets [35]. The function groups can be involved in the bonding process between RGO and molybdenum sulfide compound, forming stable chemical link as electron transfer channels to accelerate the charge separation [36]. In this regard, the heterostructures of MoS$_2$/RGO have been reported by different research groups [37–46]. For example, Jiang et al. [29] developed a PI(polyimide)/CNT(carbon nanotube)-RGO-MoS$_2$ film using RGO nanosheets as the media. The improved HER activity of such catalyst was attributed to the enormous number of active sites and fast electron transfer.

Actually, the PEC performance of MoS$_2$-RGO heterostructure was not as good as expected probably due to the flower-like microstructure or random distributed agglomeration, which could deteriorate the connectivity between RGO and MoS$_2$ [32]. It was because of the electrostatic repulsion between the negatively charged GO surface with oxygen-contained functional groups [47] and the common precursor of Mo, such as MoO_4^{2-} and $Mo_7O_{24}^{6-}$. Therefore, surface modification techniques were employed to modulate the surface states of GO/RGO to improve the interphase connectivity for forming homogeneous heterostructures [48–54]. Cationic surfactants [41] and ionic liquids [48] were introduced to modify the surface charge of GO/RGO through electrostatic and π-π interactions to generate the homogeneous nucleation of MoS$_2$ on GO or RGO surfaces. The density functional theory simulation results also indicated that the metal cations could give strong interaction with the oxidized groups on the RGO sheet [49], as well as cation–π interaction with the graphene sheet [50]. Metal ions were also employed as the bridged absorbents on RGO surface to enhance the physicochemical performance in photocatalytic and biomedical applications [51,49–54]. However, the research is absent for metal ions to act as the bridged agents and connect MoS$_2$ with conductive substrate to generate the photo-assisted electrocatalytic HER activity.

In this paper, a facile one-step in-situ hydrothermal method is developed to grow highly dispersed and vertical MoS$_2$ nanolayers on the surface of RGO photocathode using metal ions as the cross-bridged sites. Metal ions modified on oxygen-contained functional groups of RGO surface can attract the negative molybdate precursors of MoS$_2$, such as MoO_4^{2-} and $Mo_7O_{24}^{6-}$, and also act as the nucleation centers for MoS$_2$ nanosheets growing vertically on RGO substrate. PEC characterization indicates that a significant improvement in photo-assisted electrocatalytic HER activity of the metal ions cross-bridged composites can be attributed to the high amount of exposed active sites and effective separation of carries of MoS$_2$, and fast electron transfer between MoS$_2$ and RGO. This facial approach may represent a highly ordered heterostructure construction strategy to fabricate innovative catalysts for photo-assisted HER.

2. Experimental section

2.1. Materials synthesis

2.1.1. Materials

Ammonium molybdate tetrahydrate ($H_{24}Mo_7N_6O_{24}\cdot4H_2O$) and thiourea (TA, H_2NCSNH_2) were purchased from Aladdin Chemical

Reagent Co., Ltd. All the other chemical reagents (A.R.) were purchased from Sinopharm Chemical Reagent Co. and used without further purification. Distilled water was used throughout the experiments.

2.1.2. Preparation of graphene oxide

The graphene oxide (GO) sheets were synthesized from graphite powder according to the previously reported methods [54,55]. In detail, graphite (1 g) was dispersed into H_2SO_4 (98%, 55 mL) solution to form a suspension, then sodium nitrate (1 g) was dissolved into this suspension with ultrasonic vibration for 40 min to form a mixture solution. Then KMnO$_7$ (8 g) was added into this mixture solution with ultrasonic vibration for 1 h. All operations were kept at 5 ℃ in ice-bath. The well mixed solution was transferred into 45 ℃ water-bath with stirring for 45 min, and then deionized water (25 mL) was dropped and followed by another 30 min of stirring. The solution was transferred into 90 ℃ water-bath under stirring about 1 h, and then the yellow precipitation was obtained after H_2O_2 (30%, 15 mL) solution was added. The obtained yellow precipitation was transferred into HCl (10%.v/v) aqueous solution and stayed overnight without stirring. The yellow precipitation was centrifuged and washed with water and ethanol for several times until the pH ∼ 7 was reached. Then the washed precipitation was dried for overnight at 60 ℃ to achieve GO powder.

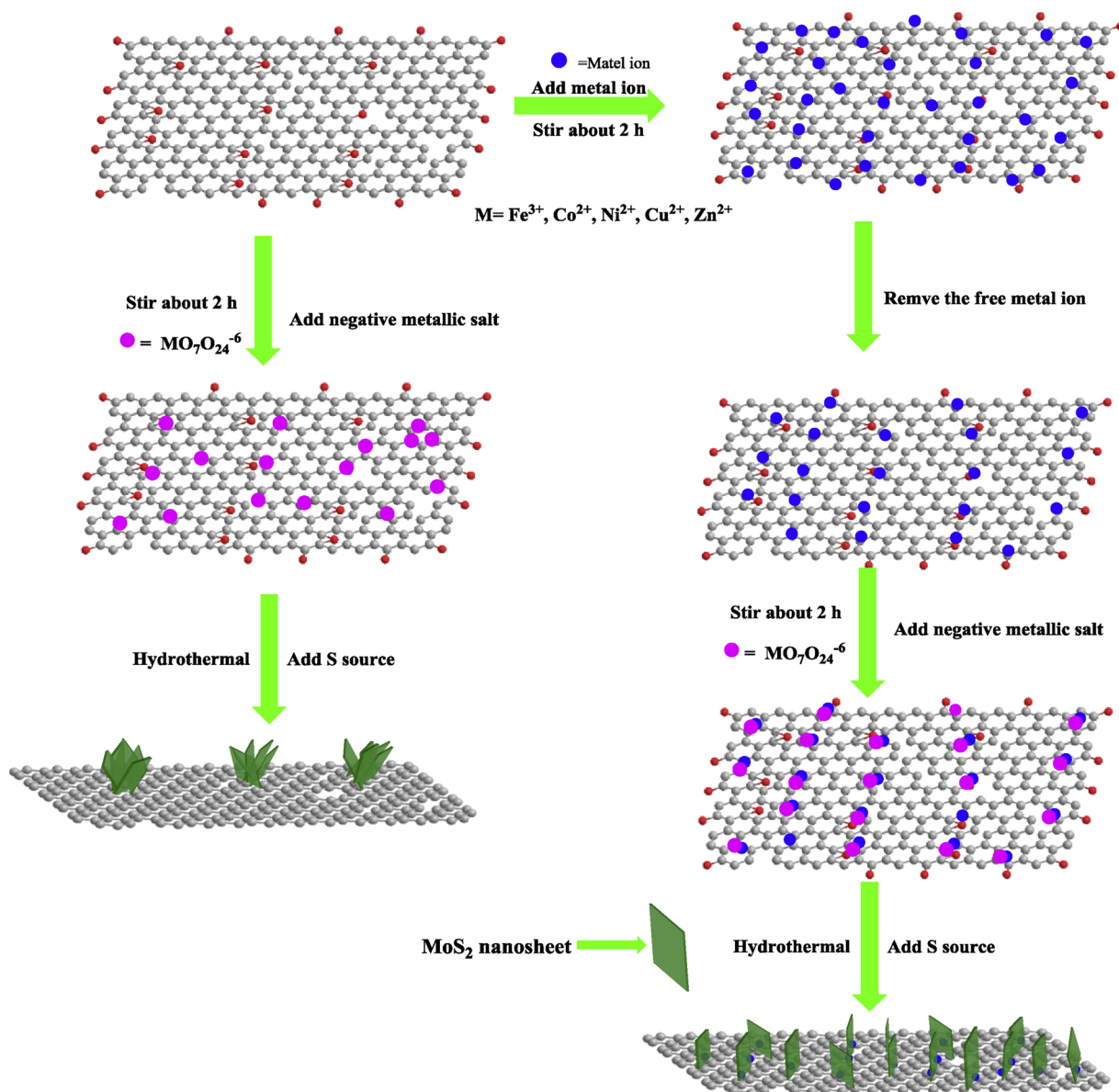#### 2.1.3. Preparation of GO-M (Fe^{3+}, Co^{2+}, Ni^{2+}, Cu^{2+} and Zn^{2+}) composites

GO powder was dispersed into deionized water with the aid of ultrasonic vibration for 40 min to from 0.5 mg mL^{-1} solution. Then different types of metal-chloride dissolved-salts (M = Fe^{3+}, Co^{2+}, Ni^{2+}, Cu^{2+} and Zn^{2+}) were added into the GO aqueous solution under stirring, respectively. The obtained mixture solutions were stirred for 2 h and stored in dark for overnight. The achieved precipitations were separately centrifuged and washed with deionized water for several times. The products were dried in vacuum oven at 50 ℃, and the powders of different metal ions decorated GO sheets (expressed as GO−M (M = Fe^{3+}, Co^{2+}, Ni^{2+}, Cu^{2+} or Zn^{2+})) were obtained.

2.1.4. Preparation of (M = Fe^{3+}, Co^{2+}, Ni^{2+}, Cu^{2+} and Zn^{2+}) RGO-M-MoS$_2$ composites

The individual GO−M (M = Fe^{3+}, Co^{2+}, Ni^{2+}, Cu^{2+} or Zn^{2+}) powder was dispersed into deionized water with the aid of ultrasonic vibration, and then the precursor of molybdate salt was injected into the GO−M aqueous solution and stirred for 2 h to form the mixture solution at room temperature. Thiourea (molar ratio $_{S:Mo}$ = 4:1) was dissolved into this mixture solution with stirring for another 1 h. The obtained mixture was transferred to a Teflon-lined autoclave and heated at 180 ℃ for 18 h in hot oven under atmospheric pressure. The product was centrifuged and washed with deionized water and then ethanol for several times. Finally, the metal-bridged RGO-M-MoS$_2$ composite powder was achieved by freeze-dried for about 24 h. The probable synthesized mechanism and procedure of the composite sample are shown in Scheme 1. According to the XPS quantification analysis (Figure S5(d)), the weight contents of metal ion (Ni) in GO−M are determined to be ca. 1.01%. For comparison, MoS$_2$ and RGO-MoS$_2$ were prepared with the same procedure without the addition of GO and/or metal ion precursor, and RGO-Ni-TA was also prepared with the same procedure without the precursor of molybdate salt.

2.2. Characterization

UV–vis absorption spectra were recorded with a UV–2600 spectrophotometer. Fourier transform infrared spectra (FTIR) were performed on a Nicolet 6700 FTIR spectrometer. Raman spectra were recorded by a (model series No. Nexus 670) Thermo Nicolet Nexus 670 spectrometer equipped with a 532 nm laser. The morphologies of the composite samples were observed on a Hitachi scanning electron microscope (SEM). TEM images were recorded with a JEOL JEM–2010 F

Scheme 1. Schematic illustration of the fabrication procedure of RGO-MoS$_2$ and RGO-M-MoS$_2$ composites.

microscope device using operating voltage at 200 kV. The composite samples were degassed at 120 °C for 6 h for N$_2$ adsorption-desorption experiments, which were carried out at 77 K on a Micrometrics Model ASAP 2020 volumetric adsorption analyzer. Powder X-ray diffraction (XRD) patterns of different samples were reported by using an X'Pert PRO diffractometer. X-ray photoelectron spectroscopy (XPS) was performed on a Thermo ESCALAB 250 X–RAY photo electron spectrometer with a monochromatic X–ray source (Al Kα hν = 1486.6 eV).

2.3. Photo-electrochemical instrumentation and measurements

Photo-electrochemical measurements were performed in a three-electrode electrochemical cell using an electrochemical workstation. Electrocatalytic performance of photocathode was recorded by a CH Instruments 660E electrochemical workstation. All measurements were performed in 0.5 M H$_2$SO$_4$ aqueous solution as electrolyte, which was purged using high purity N$_2$ gas before measurements. Glassy carbon electrodes (GCE) coated by the as-prepared composite samples were used as the working electrode (photocathode), and the Ag/AgCl electrode and Pt wire were used as the reference and counter electrodes,

respectively. The light source is a 150 W Xenon arc lamp, and the distance between the lamp and the as-prepared photocathode was 15 cm.

The individual working photocathode was made by the following steps: 4.0 mg of the composite catalyst powder was mixed into 700 μL water and 250 μL isopropyl alcohol mixture along with 50 μL of 5 wt.% of Nafion$^{®}$ solution. The formed mixture was dispersed by ultrasonic vibration for 30 min to form the homogeneous ink. Then 10 μL of the catalyst ink was loaded on a GCE (D = 3 mm) with a catalyst loading of 0.57 mg cm^{-2}.

For the electrocatalytic performance of HER test, the linear sweep voltammograms (LSV) tests were conducted in 0.5 M H$_2$SO$_4$ aqueous solution with a potential scan rate of 5 mV s^{-1}, which were performed after the cyclic voltammetry (CV) tests to stabilize the current. The long-term stability tests were carried out using a chronoamperometry technique at an overpotential of 210 mV without light illustration.

All data of the electrochemical impedance spectroscopy (EIS) were recorded with a frequency range from 0.1 to 100 kHz at an overpotential of 180 mV with an AC interrupt voltage of 5 mV. All the potentials reported in this work were referred to the reversible hydrogen electrode (RHE) by converting Ag/AgCl electrode potential to RHE. For conversion of the obtained

potential to RHE in 0.5 M H_2SO_4 [56], $E_{RHE} = E^0_{(Ag/AgCl)} + E_{(Ag/AgCl)} + 0.059$ pH, where $E^0_{(Ag/AgCl)}$ was taken to 0.210 V at pH 0.3, where the $E_{(Ag/AgCl)}$ is the work voltage during the measurements.

2.4. Computational methods

All calculations were performed within the spin-polarized density functional theory (DFT) framework as implemented in the Quantum-Espresso package [57]. Ultrasoft pseudopotentials are introduced to describe the electron-ion interactions [58]. Perdew-Burke-Ernzerhof (PBE) function in the generalized gradient approximation (GGA) was employed to describe the exchange-correlation functional [59]. The Kohn-Sham (KS) orbitals and the charge density were represented using basis sets consisting of plane waves (PWs) up to a maximal kinetic energy of 50 Ry and 400 Ry, respectively. The coupled oxidized graphene and MoS_2 nanolayer with and without Ni connectors were modelled using the supercell. The other end of MoS_2 nanolayer exposed for hydrogen adsorption was Mo-edge covered with S atoms. A vacuum space of 15 Å in the non-periodic direction was used to avoid interaction between the neighbouring images. Γ-point sampling of the Brillouin zone was adopted for the relaxation of each supercell, which was sufficient when considering their large real-space dimensions. The convergence in energy and force were set to 10^{-7} eV and 10^{-4} eV/Å.

3. Results and discussion

3.1. Microstructure

The morphologies of the prepared hybrid catalysts are shown in Fig. 1 and **Fig. 1S** by both SEM and TEM images. Fig. 1 compares the TEM images of as-prepared GO, RGO-MoS$_2$, and RGO-Ni^{2+}-MoS$_2$ samples. Particularly, the translucent GO sheets with wrinkles ultrathin can be observed in Fig. 1a. When introducing the precursor of Mo without metal ions, MoS_2 nanosheets grown on the RGO surface tend to stack into the flower-like and inhomogeneous agglomerations, as shown in **Fig. S1a** and Fig. 1b. In contrast, with the aid of the introduced Ni^{2+} ions on the surface of GO, MoS_2 nanosheets are highly ordered and

uniformly distributed on the surface of RGO, and the wrinkled MoS_2 nanosheets are interconnected with each other, as shown in **Fig. S1b** and Fig. 1c. It can be observed that most of MoS_2 sheets are more inclined to vertically grow on the surface of RGO rather than grow parallel on the surface [32,60]. As labeled in the HRTEM images (Fig. 1d), the image reveals that the interlayer spacing, 0.72 nm, is larger than that of standard MoS_2, ~0.62 nm, corresponding to the (002) crystal planes [61,62]. The expanded interlayer spacing may be due to the lattice mismatch effect between RGO and MoS_2 through the flexible connection via metal ions. The sample of RGO–M(Ni^{2+})–MoS$_2$ shows a higher BET specific surface area of 946.04 m^2 g^{-1} (**Fig. S6**) than that of RGO-MoS$_2$ (863.12 m^2 g^{-1}). The increased surface area can be ascribed to MoS_2 sheets grown vertically and uniformly on the surface of RGO with the present of metal ions, by which the enfoldment and restack of RGO nanosheets and agglomeration of MoS_2 nanosheets can be can inhabited.

3.2. Elements coordination environments

The chemical structure of the as-prepared materials MoS_2, RGO-MoS_2, RGO-Ni-TA and RGO-Ni-MoS_2 were further analyzed through Fourier transform infrared spectroscopy (Fig. 1e). The peak at 1633 cm^{-1} is attributed to C=C bond skeletal vibration of RGO sheets and C=O stretching vibration [63,64], which shifts to 1613 cm^{-1} in RGO-Ni-MoS_2 composite due to the strong interaction between Ni^{2+} and RGO surface [54]. The peaks centered at 1400 cm^{-1} can be ascribed to the C–O–H deformation, and 1200 cm^{-1} and 1031 cm^{-1} are ascribed to the C–N stretching vibration, indicating the formation of N-doped group on the surface of RGO during the hydrothermal process. The peak at 1116 cm^{-1} in RGO-MoS_2 and RGO-Ni-TA composite samples are related to the C–O–C stretching vibration, which has a red shift to 1123 cm^{-1} in RGO-Ni-MoS_2 due to the interaction between the absorbed Ni^{2+} and RGO/MoS_2. The peak near 434 cm^{-1} corresponds to the Ni–O bond [65], which can be ascribed to the binding of metal ions and oxygen atoms on the surface of RGO. The peak near 465 cm^{-1} corresponds to the Mo–S bond (**Fig. S3**) [62]. The presence of MoS_2 in the composites can also be confirmed by UV–vis diffuse reflection spectra
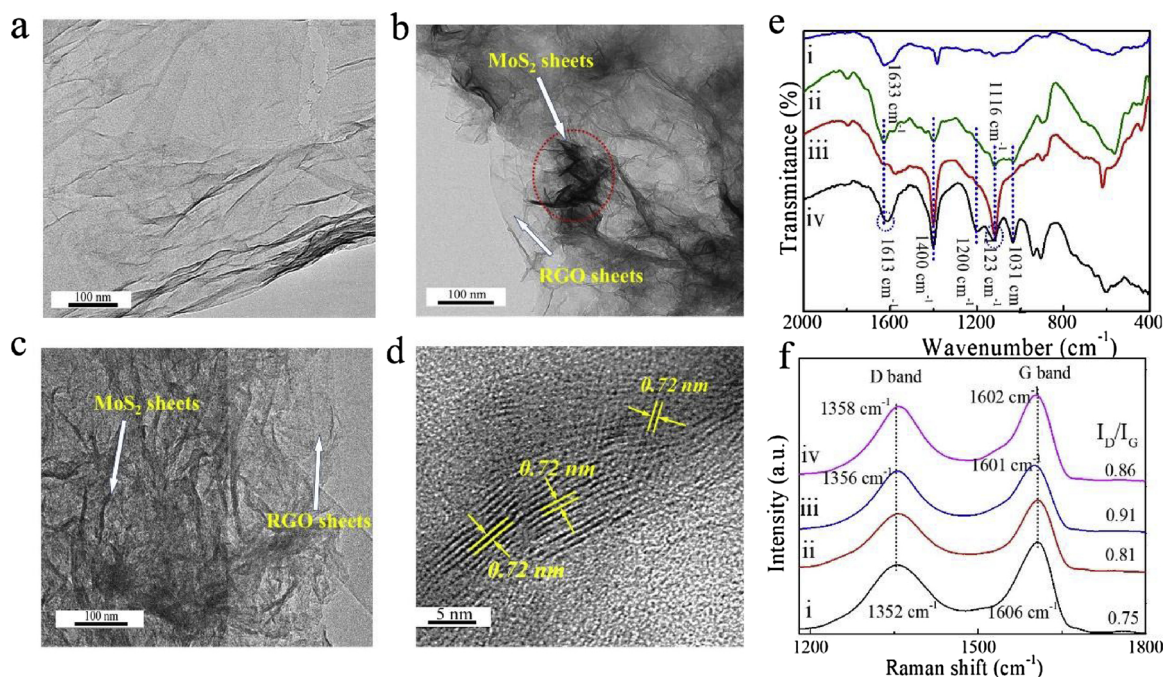

Fig. 1. TEM images of GO (a), RGO-MoS$_2$ (b) and RGO-Ni^{2+}-MoS$_2$ (c) samples and the corresponding High-resolution TEM(HRTEM) image of RGO-Ni^{2+}-MoS$_2$ composite (d). FTIR spectra (e) of MoS$_2$ (i), RGO-MoS$_2$ (ii), RGO-Ni-TA (iii) and RGO-Ni-MoS$_2$ (iv). Raman spectra (f) of GO (i), RGO (ii), RGO-MoS$_2$ (iii) and RGO-Ni-MOS$_2$ (iv) composites.

(**Fig. S2a**). **Fig. S2b** shows that the RGO nanosheets exhibit a broad (002) diffraction peak at around 2θ = 26° and the two broad and weak diffraction peaks centered at around 2θ = 33.8°, and 57.1° correspond respectively to the (100), and (110) planes of the hexagonal MoS_2 (2H MoS_2, JCPDS 37–1492).

3.3. Raman analysis

Raman spectroscopy confirms the formation of MoS_2 as indicated by the peaks located at 312 cm^{-1}, 450 cm^{-1} and 742 cm^{-1} in the low frequency domain (**Fig. S4**) [33,66]. The stretching vibration of Mo = O mode near 814 cm^{-1} is absent, indicating that the content of MoO_x is below the detect limit of Raman [66]. As shown in **Fig. 1f**, Raman spectrum of GO exhibits two characteristic peaks at 1352 cm^{-1} and 1606 cm^{-1}, which can be attributed to the graphitic D-band and G-band, respectively. The D-band originates predominantly from the defects as well as the disordered atomic arrangements, whereas the G-band evolves from the symmetric stretching of sp^2 C—C bond [67]. The I_D/I_G ratio increases from 0.75 in GO to 0.81 in RGO, demonstrating the decrease in the average size of sp^2 domains and the reduction of GO to RGO [68]. Meanwhile, the I_D/I_G ratios of the RGO-MoS_2 and RGO-Ni-MoS_2 sample were 0.91 and 0.86, respectively. Compared with GO/ RGO, the peaks of D band and G band in the RGO-MoS_2 and RGO-Ni-MoS_2 sample are both slightly shifted away due to the interaction of MoS_2 nanosheets with RGO nanosheets [67–69], which is consistent with the FTIR spectra and XPS analysis.

3.4. XPS analysis

To analyze the chemical states of RGO-M(Ni)-MoS_2 composite samples, XPS was used to obtain the specific information of individual components, as shown in **Fig. S5** and **Fig. 2**. The existence of C, O, S, N Mo and Ni elements in the nanocomposite is confirmed by the survey scan, as shown in **Fig. S5**. C and O elements are originated from RGO. S and N elements come from the hydrothermal process. Sufficient O

atoms at the surface of RGO is beneficial to the anchoring of metal ions, which offers enough bridged sites for negative charged precursor of Mo. In **Fig. 2a**, the peaks corresponding to the binding energy of Mo-O_x can be observed at 230.1 eV, 232.9 eV, 233.7 eV and 236.6 eV, due to the presence of partially oxidized MoS_2 formed after getting exposed to the air or incomplete vulcanization. The peaks observed at 228.8 eV and 231.9 eV are corresponding to the 3d$_{5/2}$ and 3d$_{3/2}$ components of Mo^{4+} in MoS_2 [70], and the peak at 226.0 eV can be assigned to S 2s. In the spectrum of S 2p (**Fig. 2b**), the peaks appeared at 162.2 eV and 163.5 eV, and the satellite peak at 168.1 eV can be attributed to the S^{2-} states in MoS_2 [11]. As shown in **Fig.2c**, the binding energy at 853.5 eV was attributed to Ni 2p$_{3/2}$, which is higher than that of reported NiS and Ni_2S_3, thus corresponding to the binding energy of the Ni–Mo [71,72]. The other peak at 856.0 eV in the Ni 2p$_{3/2}$ spectrum are assigned to Ni^{2+} 2p core level, and a satellite peak at approximately 860.0 eV corresponds to Ni (II) oxide species, which is related to the O(2p)–Ni (3d) charge-transfer transition [52,73]. The curve fit of the O 1s spectrum (**Fig. 2d**) results in four peaks located at 529.6 eV, 530.4 eV, 531.6 eV and 532.1 eV, which are assigned to the Ni–O [74], O=C—OH, C—OH and − C—O—C−, respectively [75]. And the peak at 530.6 eV corresponds to O–1s core level and is assigned to Mo−O [76]. According to the TEM, FTIR, Raman and XPS analysis, it is deduced that the uniformly distribution of Ni^{2+} on RGO surface can act as the media to connect RGO sheets and MoS_2 sheets, which then inevitably affect the formation of geometric and electronic structure of MoS_2 and exert a direct influence on the HER activity.

3.5. Model of MoS_2 growth on RGO substrate

Based on the result of TEM observation and the above analysis, the formation process of the RGO–M–MoS_2 composite with the expanded layered of MoS_2 can be illustrated in Scheme 1. First, the O atoms coming from the oxygen-containing functional groups act as the sites to anchor and collect metal ions with electrostatic and cation–π interactions, then the negative precursor of molybdenum source is captured by
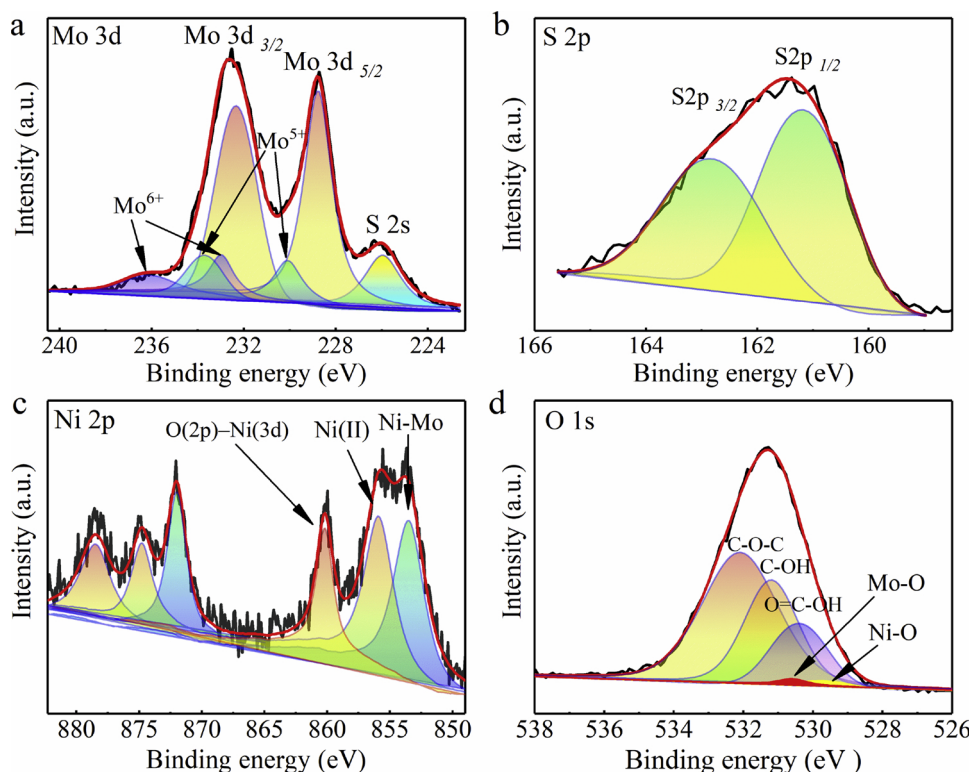

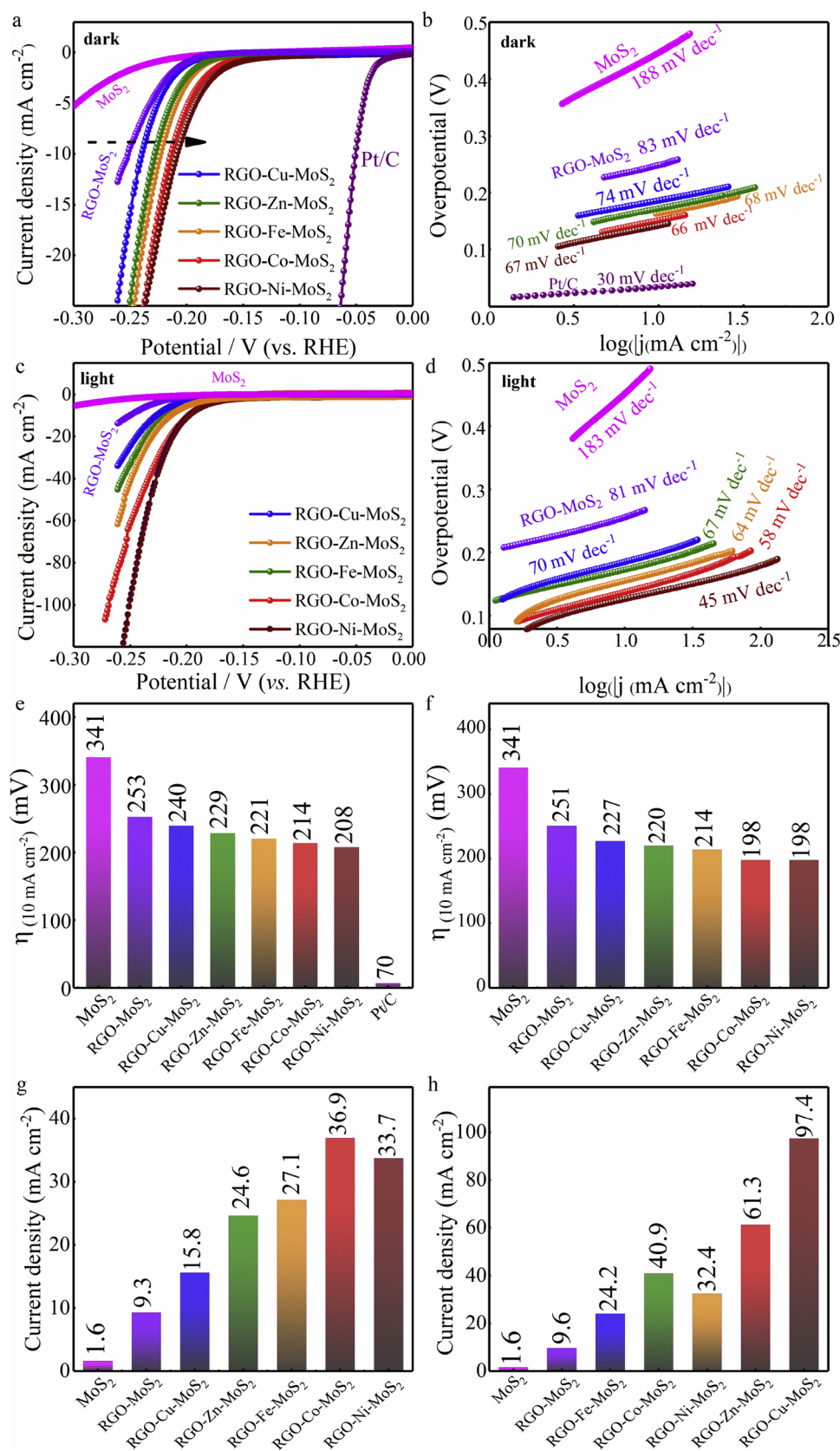**Fig. 2.** High-resolution XPS spectra of Mo 3d (a), S 2p (b), Ni 2p (c) and O 1s (d).

Fig. 3. Polarization curves obtained with various catalysts both in the dark (a) and under light illumination (c). The corresponding Tafel plots (b, d). The histogram of η at j = 10 mA cm^{-2} of various as-prepared samples under different atmospheres: dark (e) and light illustration (f). Current densities of the as-prepared samples at the overpotential of 250 mV under different atmospheres: dark (g) and light illustration (h).

the elected metal cations. The metal ions act as the linked agent between MoS_2 and RGO. Then the MoS_2 nanosheets grow up chain by chain on the surface of RGO nanosheets with the metal ion as the bridged agent during the hydrothermal process, and finally the vertically grown and uniformly distribution of expanded layered MoS_2 on the surface of RGO nanostructures are achieved. On the contrary, without adding metal ions, MoS_2 nanosheets tend to stack into the flower-like agglomerations on RGO surface as shown in Fig. 1.

3.6. Electrochemically-measured HER activity

Electrochemical performance for HER are shown in Fig. 3 to compare the photoelectrochemical HER activities of the as-prepared metal-bridged RGO and MoS_2 (RGO-M-MoS_2) catalysts. Fig. 3a and b show the polarization curves and the corresponding Tafel plots of the catalyst samples measured in darkness. It can be seen that Pt/C exhibits the lowest overpotential and obtains the highest HER activity compared to the other catalysts due to its high hydrogen adsorption (H_{ads}) coverage [77]. The HER process on the surface of Pt generally matches the Volmer-Tafel mechanism and the rate-limiting step is corresponding to recombination step and it can be attested by the measured Tafel slope of $30\,mV\,dec^{-1}$ [77]. RGO-M-MoS_2 composite catalysts show much lower overpotentials (η) at current density of $10\,mA\,cm^{-2}$ compared to that of MoS_2 and RGO-MoS_2, indicating the positive effect of metal ion addition on the performance of electrocatalytic activity. According to the DFT calculations [49], the cation-π interactions between metal ion and the graphite surface have similar behavior. However, the adsorption energy between metal ion and graphene oxide/graphene would be changed depending on the type of metal ion. Furthermore, the metal ions prefer to adsorb at the regions where oxidized groups and aromatic rings coexist. The existed oxygen-containing functional groups on the surface of reduced graphene oxide would further enhance the bonding strength between metal ion and graphene oxide/graphene [50,54], leading to the various interfacial interaction between reduced graphene oxide and MoS_2 nanosheets. Those results are also testified by the EIS measurement as Fig. 4a, which is a common method to figure out the interfacial carried charge of composites with adding different metal

ions. The composites with different metal ions affect the interaction between graphene oxide/graphene and MoS_2 nanosheets, thus leading to the changeable performance for composites via adding different metal ions. Particularly, RGO-Ni-MoS_2 obtains the lowest η (208 mV) at the current density of $10\,mA\,cm^{-2}$, implying a superior HER activity among the RGO-M-MoS_2 catalysts.

For comparison, Fig. 3c and d show the polarization curves and the corresponding Tafel plots of the samples measured under light illumination. The photocathodic current density rises rapidly under a more negative potential, as shown in Fig. 3f, compared to that of in dark shown in Fig. 3e. Particularly, comparing to the current density at the overpotential of 250 mV between the both conditions, the current densities of the catalysts modified with metal ions all achieve obvious improvement under light illumination (Fig. 3h) than that in dark (Fig. 3g). The enhanced performance of PEC water splitting for H_2 evolution is attributed to the uniformly distribution, more exposed edge sites, efficient separation of charge carries, and the excellent conductive provided by RGO generated by the unique fabrication strategy with metal ions addition [78]. The efficient separation of charge carries in the RGO-Ni-MoS_2 composite was also characterized by Fluorescence measurement as observed in Fig. S7. The remarkable quenching for the RGO-Ni-MoS_2 composite means the strong interaction between RGO and MoS_2 due to the bridging metal ion. It is demonstrated that the implantation of metal ions is able to promote the electron transfer across the interface between RGO and MoS_2. Importantly, the faster electron transfer should be advantageous to enhance the catalytic activity for water splitting into H_2.

3.7. Tafel characterization

In order to identify the HER kinetics catalyzed by the metal-bridged catalysts in darkness and under illumination, the corresponding Tafel slopes have been characterized as shown in Fig. 3b and d, respectively, which are fitted to the Tafel equation ($\eta = a + b\log j$, where j is the current density and b is the Tafel slope) [77]. In general, three principal possible steps are proposed for hydrogen evolution process on the catalyst modified electrode surface in acidic solution [79]:
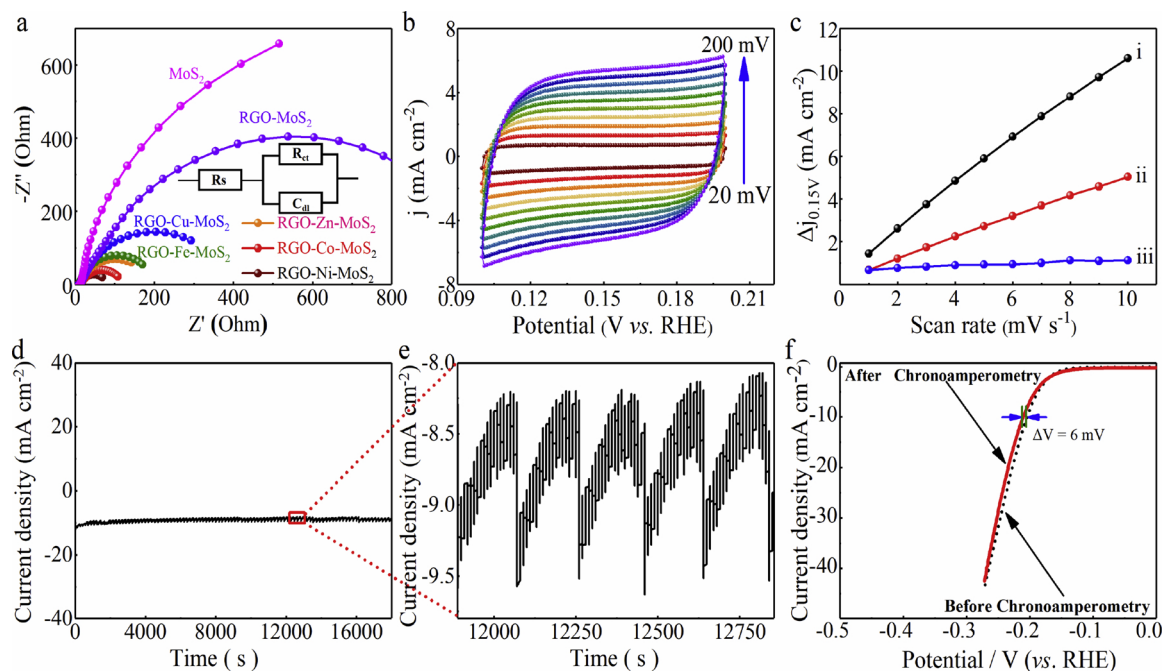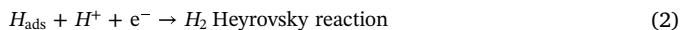

Fig. 4. Nyquist plots (a) of EIS for various electrocatalysts at the modified GCEs. Electrochemical cyclic voltammogram (b) of RGO-Ni-MoS_2 measured at different scan rates from 20 to 200 mV s^{-1} and the C_{dl} (c) of MoS_2, RGO-MoS_2 and RGO-Ni-MoS_2 catalysts obtained at 0.15 V versus RHE. Stability test of the RGO-Ni-MoS_2 electrocatalyst (d, e and f).

$$H^+ + e^- \rightarrow H_{ads} \quad \text{Volmer reaction} \tag{1}$$

$$H_{ads} + H^+ + e^- \rightarrow H_2 \; \text{Heyrovsky reaction} \tag{2}$$

$$H_{ads} + H_{ads} \rightarrow H_2 \quad \text{Tafel reaction} \tag{3}$$

According to previous literatures [66], the Tafel slope value of 30 mV dec^{-1}, 40 mV dec^{-1}, and 120 mV dec^{-1} follow the Tafel, Heyrovsky, and Volmer reaction mechanisms for the HER rate determining steps, respectively. Pt/C test as the standard with a Tafel slope of 30 mV dec^{-1} follows the known Tafel mechanism determined by the high H$_{ads}$ coverage [77]. The Tafel slopes of the as-prepared catalysts with metal ions as the bridge: RGO-Cu-MoS$_2$ (74 mV dec^{-1}), RGO-Zn-MoS$_2$ (70 mV dec^{-1}), RGO-Fe-MoS$_2$ (68 mV dec^{-1}), RGO-Co-MoS$_2$ (66 mV dec^{-1}) and RGO-Ni-MoS$_2$ (57 mV dec^{-1}) are smaller than those for pure MoS$_2$ (188 mV dec^{-1}) and RGO-MoS$_2$ (83 mV dec^{-1}), suggesting the faster electron transport of RGO-M-MoS$_2$ catalysts. Furthermore, the Tafel slopes of the samples with adding metal ions, i.e., (RGO-Cu-MoS$_2$ (70 mV dec^{-1}), RGO-Fe-MoS$_2$ (67 mV dec^{-1}), RGO-Zn-MoS$_2$ (64 mV dec^{-1}), RGO-Co-MoS$_2$ (58 mV dec^{-1}) and RGO-Ni-MoS$_2$ (45 mV dec^{-1})), show much smaller Tafel slopes under light illumination than those without illumination, suggesting that the electrochemical desorption is also the rate-limiting step in the HER catalyzed by the RGO-M-MoS$_2$ catalysts [33]. These values of Tafel slopes catalyzed by RGO-M-MoS$_2$ indicate that the reactions follow the Volmer-Heyrovsky mechanism [77]. Both **Eq.** (1) and (2) are operative in the HER catalyzed by RGO-M-MoS$_2$ composites due to their similarity in surface chemical properties and the path of electron transport even their morphologies are different. Comparing the performance of RGO-M-MoS$_2$ composites with those of other reported MoS$_2$-based catalysts as shown in **Table S3**, it can be seen that RGO-M-MoS$_2$ catalysts show relatively low Tafel slopes and η (10 and 100 mA cm^{-2}) values. These electrochemical results and above instrument characterization indicate that metal ion bridge can create more exposed edges and higher efficient of electron transfer in RGO-M-MoS$_2$ catalysts, which provide more active sites and smooth path for HER, resulting in larger catalytic current at low overpotential.

3.8. Exchange current density

The exchange current densities (j_0) of MoS$_2$, RGO-MoS$_2$, RGO-Ni-MoS$_2$ and Pt/C were calculated from Tafel plots using the extrapolation methods and shown in **Fig. S8** and **Table S1**. It can be seen that RGO-Ni-MoS$_2$ composite catalyst exhibits the higher exchange current density (j_0) of 0.0776 mA cm^{-2} than the pristine MoS$_2$ (0.0151 mA cm^{-2}) and RGO-MoS$_2$ (0.0347 mA cm^{-2}), indicating the higher catalytic activity towards HER of this RGO-Ni-MoS$_2$ catalyst.

3.9. EIS measurements

EIS measurements were carried out to characterize the interface reactions and electrode kinetics of the catalysts toward HER. Nyquist plots of the as-prepared materials are given in **Fig. 4a** with the corresponding electrical equivalent circuit for fitting the EIS experimental data according to the model of the simple Randle's cell (**Fig. 4a** inserted). The working cathodes coated by various catalysts exhibit a similar semicircle, indicating that the corresponding equivalent circuit for the HER can be characterized by one time constant, and the reaction is controlled by reaction kinetics [80]. The smaller radius of semicircle is obtained by adding metal ion as the bridging agents, then the RGO-Ni-MoS$_2$ presents the lower charge transfers resistance (R_{ct}) of 70.4 Ω, which is much smaller than those of MoS$_2$ (> 1200 Ω) and RGO-MoS$_2$ (1040.1 Ω), as shown in **Table S2**. The lower R_{ct} value of the RGO-Ni-MoS$_2$ is beneficial to the enhancement of electron transfer process by decreasing the charge recombination rate. R_{ct} is related to the electrocatalytic kinetics and the low value corresponds to the high HER reaction rate [29,62,81]. Additionally, the semicircles for the composite

catalysts with adding metal ions are all much smaller than that of pristine MoS$_2$ and RGO-MoS$_2$, suggesting the rather low R_{ct} between the solid-liquid interface for RGO-M-MoS$_2$ cathodes. This is because of the effectively exposes of catalytically active MoS$_2$ edges to electrolyte. The results above are in good agreement with the HER and Tafel slope results shown in **Fig. 3**. It can be concluded that the enhanced photoelectrocatalytic properties of RGO-M-MoS$_2$ may be contributed to the strong chemical and electronic interactions between RGO and MoS$_2$ due to the addition of metal ions. This addition of metal ions can generate the metal ion bridging structures, as confirmed by Raman, FTIR and XPS analysis, resulting in the efficient charge transfer between the catalytic edge sites and the conductive support.
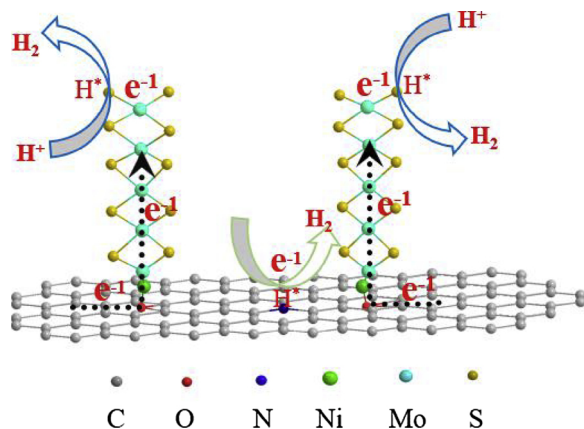
3.10. Effective electrode surface area

Electrochemical double-layer capacitance has strong correlation with the HER catalysis and electrochemical area of MoS$_2$, RGO-MoS$_2$ and RGO-M-MoS$_2$. As shown in Fig. 4b and **Fig. S10**, the cyclic voltammetry is employed to estimate the effective electrode surface area for HER [82]. Fig. 4c shows that the capacitance of RGO-Ni-MoS$_2$ (25.7 m F cm^{-2}) is around 10 times and 2 times larger than those of MoS$_2$ nanoparticles (2.7 m F cm^{-2}) and RGO-MoS$_2$ (12.1 m F cm^{-2}), indicating the highest exposure of effective active sites can be achieved due to the vertical grown of interlayer-expanded MoS$_2$ nanosheets and high specific surface area, resulting in excellent HER activity as shown in Fig. 3 [83].

3.11. Cycling performance

To evaluate the electrochemical durability of the composite catalysts, a long-term HER test was conducted at 10 mA cm^{-2} in 0.5 M H$_2$SO$_4$ aqueous solution. As shown in Fig. 4d, the RGO-Ni-MoS$_2$ composite have a relatively stable overpotential at 10 mA cm^{-2} for 18000 s in acidic solution, indicating their good long-term operating stability during the HER process. A small sawtooth fluctuation under the durability test (the amplified red area in Fig. 4d) reflecting the decreasing and increasing of current density can be attributed to the periodic formation and release of H$_2$ bubbles on the electrode. The bubbles on the surface of RGO-Ni-MoS$_2$ composite catalyst can release easily, due to the vertically grown, highly ordered and uniformly distributed MoS$_2$ nanosheets on the surface of RGO. However, the RGO-MoS$_2$ composite shows violent sawtooth fluctuation under the durability test (**Fig. S11**) because the bubbles formed on the surface of electrode are difficult to release due to the aggregation and random distribution of MoS$_2$ nanoparticles on the surface of RGO, as indicated by the TEM analysis. Furthermore, the stability test of the composite catalyst toward HER is compared between the former test of chronopotentiometry and the later one (Fig. 4e). According to Fig. 4d and e, the RGO-Ni-MoS$_2$ catalyst shows high HER durability in acidic solution.

3.12. Proposed HER scheme

According to the analysis by HRTEM images and FTIR, Raman, XPS spectra, and electrochemical measurements, the excellent electrochemical performance can be attributed to the metal ion bridged structures of RGO-M-MoS$_2$ composite catalysts. As illustrated in Scheme 2, taken Ni ion as an example, the advantages of the prepared electrodes are possible as follows: First, MoS$_2$ nanosheets with expanded interlayer spacing grow vertically on RGO nanosheets, which provides abundant active edge sites for HER and a shorter diffusion distance for hydrogen gas overflow; second, the strong interaction and stable structure can result in long-term durability for HER. Ni ion locating at the interfacial between RGO and MoS$_2$ also provides a smooth electron transfer path between MoS$_2$ and RGO [52,84]. And third, MoS$_2$, as a semiconductor photocatalyst, the photogenerated electron can also transfer from MoS$_2$ nanosheets to the surface of RGO under light

Scheme 2. Schematic illustration showing the possible electron transfer paths for photo-assisted electrocatalytic HER in the RGO-M(Ni^{2+})-MoS$_2$ electrode.

illustration, which may further enhance the catalytic active with active sites attributing to N-doping on the surface of RGO among hydrothermal process. On the other hand, the photogenerated electron can also be utilized in the surface of MoS$_2$ during photo-electrocatalytic process. Thus, RGO-Ni-MoS$_2$ catalyst displays a high catalytic performance and long-term durability.

3.13. Hydrogen coverage

To further investigate the high electrocatalytic activity of the designed catalysts, DFT calculations were used to get a fundamental understanding of the electrocatalytic activity [85–89]. Theoretically, the HER pathway in acidic media can be described by the following three steps: an initial state $H^+ + e^-$, an intermediate adsorbed H^*, and a final product 1/2H_2 (**Fig. 5a**). $\triangle G_{H*}$ is one of the key points in theoretical prediction of the HER activity [80], which can be calculated by the following **Eq.** (4).

$$\Delta G_{H*} = \Delta E_{H*} + \Delta E_{ZPE} - T\Delta S \tag{4}$$

where ΔE_{H*} is the hydrogen adsorption energy, and ΔE_{ZPE} is the difference between the adsorbed state and the gas phase with respect to the zero-point energy (ZPE). As the vibrational entropy of H^* in the adsorbed state is small, the entropy of ½H_2 adsorption is: $\Delta S_H \approx -\frac{1}{2}S^0_{H_2}$, where $S^0_{H_2}$ is the entropy of H_2 in the gas phase at the standard conditions. Therefore, the overall corrections are expressed by **Eq.** (5).

$$\Delta G_{H*} = \Delta E_{H*} + 0.24 eV \tag{5}$$

Previous studies have used $|\triangle G_{H*}|$ as a catalytic descriptor for HER and proposed the optimal value of ~ 0 [86], by which a fast formation of adsorbed hydrogen and a rapid concomitant hydrogen release can be realized. The ΔG_{H*} depends on the dynamic processes of H^* absorption and release because hydrogen evolution rate is determined by the participation proportion of active sites, i.e., the coverage of H^* on the potential active sites. Fig. 5a compares the calculated $\triangle G_{H*}$ variation with different H^* coverages of the exposed sulfur ions on RGO-Ni-MoS$_2$ edge with θ_{H*} = 1/3, 1/2, 2/3, and 1, respectively. The values of the calculated ΔG_{H*} are changed with different degrees of H^* coverage. In addition to the ZPE and the entropy effect on the differential free energy, non-local correlation effects from adsorbed H* atoms also make a difference, among which fully covered MoS$_2$ edge in RGO-Ni-MoS$_2$ structure present the most superior electrocatalytic performance with a ΔG_{H*} value almost to zero [90]. Metal ions, as the medium in the RGO-MoS$_2$ composite catalysts, not only can facilitate the uniformly distribution of MoS$_2$ nanosheets on the RGO, but also serve the nuclear centers for vertically growth of MoS$_2$ nanosheets. However, without metal ions, MoS$_2$ nanosheets grown on the RGO surface tend to stack into the flower-like and inhomogeneous agglomerations. The expanded layer and vertically growth of MoS$_2$ on the surface of RGO with lager effective surface area can offer more active sites for H^* coverage (θ_{H*}). Meanwhile, the experimental results also show that RGO-MoS$_2$ with small amount of Ni ion as the medium can lead to highly active electrocatalyst comparable to RGO-MoS$_2$ catalyst without metal ions.

3.14. HER free-energy diagram

The value for the well-known highly efficient Pt catalyst is near-zero as $|\triangle G_{H*}|$ = 0.09 eV. [82] MoS$_2$ has the proper $|\triangle G_{H*}|$ of 0.07 eV, while its poor conductivity and inert basal plane restrain the performance of HER [18]. RGO, as the substrate of the composite, shows the high $\triangle G_{H*}$ value of 2.6 eV [91], indicating a weak H^* adsorption and easy product desorption, resulting in non-ideal performance of HER. RGO-Ni-MoS$_2$ obtains the smallest $|\triangle G_{H*}|$ value of 0.18 eV, as shown in Fig. 5b, indicating the best electrocatalytic activity from the viewpoint of thermodynamics. On the contrary, RGO-MoS$_2$ has the $\triangle G_{H*}$ value of -0.33 eV. This relatively larger negative $\triangle G_{H*}$ on RGO-MoS$_2$ indicates that chemical adsorption of H^* on its surface is strong, which is unfavourable for the following H* desorption from the actively adsorbed site and being released for an efficient electrocatalytic HER [87]. In contrast to a non-local VdW interaction between graphene and vertically aligned MoS$_2$ layer (**Fig. S9**), a number of electrons can be easily transferred from graphene to catalytically active MoS$_2$ layer via the bridging-Ni atom, which can efficiently reduce the edge adsorbed H^* species and facilitate its transformation to final molecular hydrogen [91]. The calculated result is consistent with the experimental results, proving that the high HER activity originates from the metal ion addition.
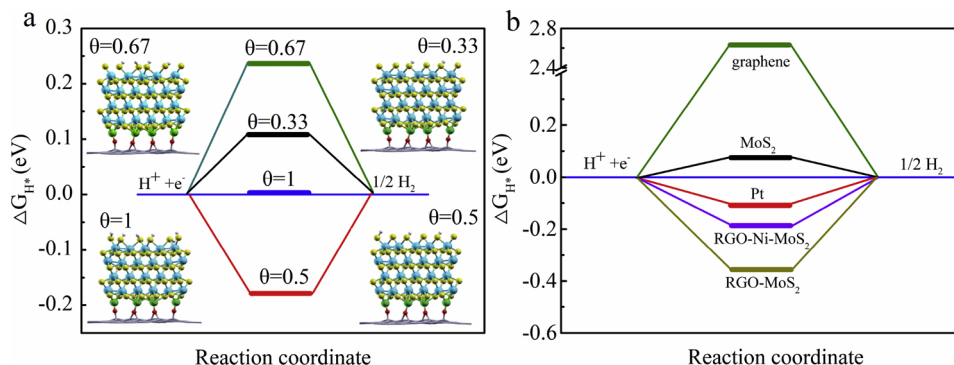

Fig. 5. (a) Free-energy diagram of HER on the surface of RGO-Ni-MoS$_2$ catalyst under different H^* coverage (1/3, 1/2, 2/3 and 1 with the molecular configurations shown as insets) conditions. (b) The calculated free-energy diagram of HER for catalysts and Pt reference.

4. Conclusions

Our study suggests that the bridging transition metal ions can result in the strong chemical coupling of the layered RGO and MoS_2, forming a robust and highly efficient RGO-M-MoS_2 photocatalyst with stable HER performance. Experimental analysis in combination with DFT calculations indicate that the improved proton reduction kinetics is responsible for the superior photo-electrocatalytic properties because of the ultra-fast electron transfer from RGO to MoS_2 through the bridging transition metal ions. Furthermore, the vertical assembly of MoS_2 on RGO substrates features the electron acceptance from RGO via the edges of the layered MoS_2 and the exposure of the most active edged S ions to enhance the proton absorption. The results may shed light on the design of high charge carrier transfer photo-eletrocatalyst based on the employment of highly conductive bridging agents.

Acknowlegdements

Appendix A. Supplementary data

Supplementary material related to this article can be found, in the online version, at doi:https://doi.org/10.1016/j.apcatb.2019.01.047.

References

[1] L. Guo, Z. Yang, K. Marcus, Z. Li, B. Luo, L. Zhou, X. Wang, Y. Du, Y. Yang, Energy Environ. Sci. 11 (2018) 106–114.
[2] E.E. Benson, H. Zhang, S.A. Schuman, S.U. Nanayakkara, N.D. Bronstein, S. Ferrere, J.L. Blackburn, E.M. Miller, J. Am. Chem. Soc. 140 (2018) 441–450.
[3] T.F. Jaramillo, K.P. Jã¸Rgensen, J. Bonde, J.H. Nielsen, S. Horch, I. Chorkendorff, Science 317 (2007) 100–102.
[4] Y. Hou, B.L. Abrams, P.C.K. Vesborg, M.E. Bjorketun, K. Herbst, L. Bech, A.M. Setti, C.D. Damsgaard, T. Pedersen, O. Hansen, J. Rossmeisl, S. Dahl, J.K. Norskov, I. Chorkendorff, Nat. Mater. 10 (2011) 434–438.
[5] K. Yamauchi, S. Masaoka, K. Sakai, J. Am. Chem. Soc. 131 (2009) 8404–8406.
[6] E. Kemppainen, A. Bodin, B. Sebok, T. Pedersen, B. Seger, B. Mei, D. Bae, P.C.K. Vesborg, J. Halme, O. Hansen, P.D. Lunda, I. Chorkendorff, Energy Environ. Sci. 8 (2015) 2991–2999.
[7] T. Wang, J. Zhuo, K. Du, B. Chen, Z. Zhu, Y. Shao, M. Li, Adv. Mater. 26 (2014) 3761–3766.
[8] L. Wang, X. Duan, G. Wang, C. Liu, S. Luo, S. Zhang, Y. Zeng, Y. Xu, Y. Liu, X. Duan, Appl. Catal. B: Environ. 186 (2016) 88–96.
[9] L. Wang, X. Liu, J. Luo, X. Duan, J. Crittenden, C. Liu, S. Zhang, Y. Pei, Y. Zeng, X. Duan, Angew. Chem. Int. Ed. 56 (2017) 7610–7614.
[10] Y. Yu, S.Y. Huang, Y. Li, S.N. Steinmann, W. Yang, L. Cao, Nano Lett. 14 (2014) 553–558.
[11] Y. Kim, D.H.K. Jackson, D. Lee, C. Min, T.W. Kim, S.Y. Jeong, H.J. Chae, H.W. Kim, N. Park, H. Chang, Adv. Funct. Mater. 27 (2017) 1701825.
[12] J. Xie, J. Zhang, S. Li, F. Grote, X. Zhang, H. Zhang, R. Wang, Y. Lei, B. Pan, Y. Xie, J. Am. Chem. Soc. 136 (2013) 17881–17888.
[13] B. Hinnemann, P.G. Moses, J. Bonde, K.P. Joergensen, J.H. Nielsen, S. Horch, I. Chorkendorff, J.K. Nørskov, J. Am. Chem. Soc. 127 (2005) 5308–5309.
[14] Y. Li, K. Yin, L. Wang, X. Lu, Y. Zhang, Y. Liu, D. Yan, Y. Song, S. Luo, Appl. Catal. B: Environ. 239 (2018) 537–544.
[15] J. Hu, B. Huang, C. Zhang, Z. Wang, Y. An, D. Zhou, H. Lin, M.K.H. Leung, S. Yang, Energy Environ. Sci. 10 (2017) 593–603.
[16] X. Huang, M. Leng, W. Xiao, M. Li, J. Ding, T.L. Tan, W.S.V. Lee, J. Xue, Adv. Funct. Mater. 27 (2017) 1604943.
[17] Y.J. Tang, Y. Wang, X.L. Wang, S.L. Li, W. Huang, L.Z. Dong, C.H. Liu, Y.F. Li, Y.Q. Lan, Adv. Energy Mater. 6 (2016) 1600116.
[18] J. Xie, H. Zhang, S. Li, R. Wang, X. Sun, M. Zhou, J. Zhou, X.W. Lou, Y. Xie, Adv. Mater. 25 (2013) 5807–5813.
[19] Y. Xue, Q. Zhang, W. Wang, H. Cao, Q. Yang, L. Fu, Adv. Energy Mater. 7 (2017) 1602684.
[20] H. Li, Y. Ke, L. Chao, T. Zheng, B. Guo, L. Xiang, F. Hao, Z. Zhu, Sci. Rep. 5 (2015) 18730.
[21] S.S. Chou, N. Sai, P. Lu, E.N. Coker, S. Liu, K. Artyushkova, T.S. Luk, B. Kaehr, C.J. Brinker, Nat. Commun. 6 (2015) 8311.
[22] Y. Yan, R.W. Crisp, J. Gu, B.D. Chernomordik, G.F. Pach, A.R. Marshall, J.A. Turner, M.C. Beard, Nat. Energy 2 (2017) 17052.
[23] R.K. Biroju, D. Das, R. Sharma, S. Pal, L.P.L. Mawlong, K. Bhorkar, P.K. Giri, A.K. Singh, T.N. Narayanan, ACS Energy Lett. 2 (2017) 1355–1361.
[24] Y. Li, L. Wang, T. Cai, S. Zhang, Y. Liu, Y. Song, X. Dong, L. Hu, Chem. Eng. J. 321 (2017) 366–374.
[25] Y. Shi, Y. Zhou, D.R. Yang, W.X. Xu, C. Wang, F.B. Wang, J.J. Xu, X.H. Xia, H.Y. Chen, J. Am. Chem. Soc. 139 (2017) 15479–15485.
[26] X. Geng, W. Wu, N. Li, W. Sun, J. Armstrong, A. Al-Hilo, M. Brozak, J. Cui, T.P. Chen, Adv. Funct. Mater. 24 (2015) 6123–6129.
[27] K. Pramoda, U. Gupta, M. Chhetri, A. Bandyopadhyay, S.K. Pati, C.N. Rao, ACS Appl. Mater. Interfaces 9 (2017) 10664–10672.
[28] K. Pramoda, U. Gupta, I. Ahmad, R. Kumar, C.N.R. Rao, J. Mater. Chem. A Mater. Energy Sustain. 4 (2016) 8989–8994.
[29] Y. Jiang, X. Li, S. Yu, L. Jia, X. Zhao, C. Wang, Adv. Funct. Mater. 25 (2015) 2693–2700.
[30] D. Lu, H. Wang, X. Zhao, K.K. Kondamareddy, J. Ding, C. Li, P. Fang, ACS Sustainable. Chem. Eng. 5 (2017) 1436–1445.
[31] L.X. Chen, F. He, N.Q. Zhao, R.S. Guo, Appl. Surf. Sci. 420 (2017) 669–680.
[32] Q. Quan, S.J. Xie, B. Weng, Y. Wang, Y.J. Xu, Small 14 (2018) 1704531.
[33] Y. Li, H. Wang, L. Xie, Y. Liang, G. Hong, H. Dai, J. Am. Chem. Soc. 133 (2011) 7296.
[34] Y. Liu, Y. Zhu, X. Fan, S. Wang, Y. Li, F. Zhang, G. Zhang, W. Peng, Carbon 121 (2017) 163–169.
[35] D.R. Dreyer, S. Park, C.W. Bielawski, R.S. Ruoff, Chem. Soc. Rev. 39 (2009) 228–240.
[36] R. Vinoth, S.G. Babu, V. Bharti, V. Gupta, M. Navaneethan, S.V. Bhat, C. Muthamizhchelvan, P.C. Ramamurthy, C. Sharma, D.K. Aswal, Sci. Rep. 7 (2017) 43133.
[37] K. Chang, W.X. Chen, ACS Nano 5 (2011) 4720–4728.
[38] S. Bertolazzi, D. Krasnozhon, A. Kis, ACS Nano 7 (2013) 3246–3252.
[39] K. Roy, M. Padmanabhan, S. Goswami, T.P. Sai, G. Ramalingam, S. Raghavan, A. Ghosh, Nat. Nanotechnol. 8 (2013) 826.
[40] L. Yu, Y.H. Lee, X. Ling, E.J. Santos, Y.C. Shin, Y. Lin, M. Dubey, E. Kaxiras, J. Kong, H. Wang, Nano Lett. 14 (2014) 3055–3063.
[41] G. Huang, T. Chen, W. Chen, Z. Wang, K. Chang, L. Ma, F. Huang, D. Chen, J.Y. Lee, Small 9 (2013) 3693–3703.
[42] C.B. Ma, X. Qi, B. Chen, S. Bao, Z. Yin, X.J. Wu, Z. Luo, J. Wei, H.L. Zhang, H. Zhang, Nanoscale 6 (2014) 5624–5629.
[43] Z.H. Deng, L. Li, W. Ding, K. Xiong, Z.D. Wei, Chem. Commun. (Camb.) 51 (2015) 1893–1896.
[44] L. Jiang, B. Lin, X. Li, X. Song, H. Xia, L. Li, H. Zeng, ACS Appl. Mater. Interfaces 8 (2016) 2680–2687.
[45] H. Long, A. Harley-Trochimczyk, T. Pham, Z. Tang, T. Shi, A. Zettl, C. Carraro, M.A. Worsley, R. Maboudian, Adv. Funct. Mater. 26 (2016) 5158–5165.
[46] Y.F. Wang, D.L. Chen, X. Yin, P. Xu, F. Wu, M. He, ACS Appl. Mater. Interfaces 7 (2015) 26226–26234.
[47] D. Li, M.B. Müller, S. Gilje, R.B. Kaner, G.G. Wallace, Nat. Nanotechnol. 3 (2008) 101–105.
[48] L. Ma, J. Ye, W. Chen, J. Wang, R. Liu, J.Y. Lee, ChemElectroChem 2 (2015) 538–546.
[49] G. Shi, J. Liu, C. Wang, B. Song, Y. Tu, J. Hu, H. Fang, Sci. Rep. 3 (2013) 3436.
[50] L. Chen, G.S. Shi, J. Shen, B.Q. Peng, B.W. Zhang, Y.Z. Wang, F.G. Bian, J.J. Wang, D.Y. Li, Z. Qian, G. Xu, G.P. Liu, J.R. Zeng, L.J. Zhang, Y.Z. Yang, G.Q. Zhou, M.H. Wu, W.Q. Jin, J.Y. Li, H.P. Fang, Nature 550 (2017) 380–383.
[51] H.P. Cong, P. Wang, S.H. Yu, Small 10 (2014) 448–453.
[52] N. Zhang, M.Q. Yang, Z.R. Tang, Y.J. Xu, ACS Nano 8 (2014) 623–633.
[53] X. Liu, J. Yang, W. Zhao, Y. Wang, Z. Li, Z. Lin, Small 12 (2016) 4077–4085.
[54] R.Y. Ge, X.Q. Li, S.Z. Kang, L.X. Qin, G.D. Li, Appl. Catal. B: Environ. 187 (2016) 67–74.
[55] W.S.H. Jr, R.E. Offeman, J. Am. Chem. Soc. 80 (1958) 1339.
[56] A. Dutta, A.K. Samantara, S.K. Dutta, B.K. Jena, N. Pradhan, ACS Energy Lett. 1 (2016) 169–174.
[57] P. Giannozzi, S. Baroni, N. Bonini, M. Calandra, R. Car, C. Cavazzoni, D. Ceresoli, G.L. Chiarotti, M. Cococcioni, I. Dabo, J. Phys. Condens. Matter 21 (2012) 395502.
[58] D. Vanderbilt, Phys. Rev. B Condens. Matter Mater. Phys. 41 (1990) 7892.
[59] J.P. Perdew, K. Burke, M. Ernzerhof, Phys. Rev. Lett. 77 (1996) 3865–3868.
[60] D. Kong, H. Wang, J.J. Cha, M. Pasta, K.J. Koski, J. Yao, Y. Cui, Nano Lett. 13 (2013) 1341–1347.
[61] O. Landon, C. Rachel, H. Trevor, A.P. Cohn, S. Keith, S. Benjamin, C.L. Pint, Nat. Commun. 7 (2016) 11796.
[62] X. Zheng, J. Xu, K. Yan, H. Wang, Z. Wang, S. Yang, Chem. Mater. 26 (2014) 2344–2353.
[63] P.F. Wang, S.H. Zhan, Y.G. Xia, S.L. Ma, Q.X. Zhou, Y. Li, Appl. Catal. B: Environ. 207 (2017) 335–346.
[64] C. Nethravathi, M. Rajamathi, Carbon 46 (2008) 1994–1998.

[65] K. Nakamoto, C. Udovich, J. Takemoto, J. Am. Chem. Soc. 92 (1970) 3973–3976.
[66] S. Kamila, B. Mohanty, A.K. Samantara, P. Guha, A. Ghosh, B. Jena, P.V. Satyam, B.K. Mishra, B.K. Jena, Sci. Rep. 7 (2017) 8378.
[67] L. Liu, Z. Liu, A. Liu, X. Gu, C. Ge, F. Gao, L. Dong, ChemSusChem 7 (2014) 618–626.
[68] G.K. Pradhan, D.K. Padhi, K.M. Parida, ACS Appl. Mater. Interfaces 5 (2013) 9101–9110.
[69] W.X. Zou, L. Zhang, L.C. Liu, X.B. Wang, J.F. Sun, S.G. Wu, Y. Deng, C.J. Tang, F. Gao, L. Dong, Appl. Catal. B: Environ. 181 (2015) 495–503.
[70] Y. Cheng, S. Lu, F. Liao, L. Liu, Y. Li, M. Shao, Adv. Funct. Mater. 27 (2017) 1700359.
[71] W. Lai, Z. Chen, J. Zhu, L. Yang, J. Zheng, X. Yi, W. Fang, Nanoscale 8 (2016) 3823–3833.
[72] A. Zhang, R. He, H.P. Li, Y.J. Chen, T.Y. Kong, K. Li, H.X. Ju, J.F. Zhu, W.G. Zhu, J. Zeng, Angew. Chem. Int. Ed. 57 (2018) 10954–10958.
[73] L.M. Yang, Z.L. Chen, D. Cui, X.B. Luo, B. Liang, L.X. Yang, T. Liu, A.J. Wang, S.L. Luo, Chem. Eng. J. 359 (2019) 894–901.
[74] S. Mu, D. Wu, Y. Wang, Z. Wu, X. Yang, W. Yang, ACS appl. Mater. Interfaces 2 (2010) 111–118.
[75] M. Gopiraman, S.G. Babu, Z. Khatri, W. Kai, Y.A. Kim, M. Endo, R. Karvembu, I.S. Kim, J. Phys. Chem. C 117 (2013) 23582–23596.
[76] S.W. Cho, L.F.J. Piper, A. Demasi, A.R.H. Preston, K.E. Smith, K.V. Chauhan, R.A. Hatton, T.S. Jones, J. Phys. Chem. C 114 (2010) 18252–18257.
[77] Y. Yan, B.Y. Xia, Z.C. Xu, X. Wang, ACS Catal. 4 (2014) 1693–1705.
[78] Y. Sun, F. Alimohammadi, D. Zhang, G. Guo, Nano Lett. 17 (2017) 1963–1969.
[79] D.Y. Chung, S.K. Park, Y.H. Chung, S.H. Yu, D.H. Lim, N. Jung, H.C. Ham, H.Y. Park, Y. Piao, S.J. Yoo, Nanoscale 6 (2014) 2131–2136.
[80] L. Liao, J. Zhu, X. Bian, L. Zhu, M.D. Scanlon, H.H. Girault, B. Liu, Adv. Funct. Mater. 23 (2013) 5326–5333.
[81] J.L. Dong, U.N. Maiti, J. Lim, S.C. Dong, W.J. Lee, Y. Oh, G.Y. Lee, O.K. Sang, Nano Lett. 14 (2014) 1228–1233.
[82] D. Kong, H. Wang, Z. Lu, Y. Cui, J. Am. Chem. Soc. 136 (2014) 4897–4900.
[83] Y. Yang, H. Fei, G. Ruan, C. Xiang, J.M. Tour, Adv. Mater. 26 (2014) 8163–8168.
[84] H. Hayashi, I.V. Lightcap, M. Tsujimoto, M. Takano, T. Umeyama, P.V. Kamat, H. Imahori, J. Am. Chem. Soc. 133 (2011) 7684–7687.
[85] J.K. Nørskov, T. Bligaard, J. Rossmeisl, C.H. Christensen, Nat. Chem. 1 (2009) 37–46.
[86] G. Zhou, Y. Shan, Y.Y. Hu, X.Y. Xu, L.Y. Long, J.L. Zhang, J. Dai, J.H. Guo, J.C. Shen, S. Li, L.Z. Liu, X.L. Wu, Nat. Commun. 9 (2018) 3366.
[87] Y. Zheng, Y. Jiao, Y. Zhu, L.H. Li, Y. Han, Y. Chen, A. Du, M. Jaroniec, S.Z. Qiao, Nat. Commun. 5 (2014) 3783.
[88] T. Liao, L.Z. Kou, A.J. Du, Y.T. Gu, Z.Q. Sun, J. Am. Chem. Soc. 140 (2018) 9159.
[89] T. Liao, Z.Q. Sun, C.H. Sun, S.X. Dou, D.J. Searles, Sci. Rep. 4 (2014) 6256.
[90] E. Skúlason, V. Tripkovic, M.E. Björketun, S. Gudmundsdóttir, G. Karlberg, J. Rossmeisl, T. Bligaard, H. Jónsson, J.K. Nørskov, J. Phys. Chem. C 114 (2010) 18182–18197.
[91] J. Su, Y. Yang, G. Xia, J. Chen, J. Peng, Q. Chen, Nat. Commun. 8 (2017) 14969.